

Supporting information

Interfacial Ionic and Thermal Regulation for Highly Reversible and Ultra-Reliable Zinc-Ion Batteries

Mengcheng Huang, ‡^a Yaojie Lei, ‡^b Yajun Hu, ^a Wei-Hong Lai, ^c Yun-Xiao Wang, ^c Chunyu Liu, ^a Shengli Zhai*^a, and Guoxiu Wang*^b

^a Key Laboratory of Eco-Textiles, College of Textile Science and Engineering, Jiangnan University, Wuxi, 214122, Jiangsu, China

^b Centre for Clean Energy Technology, School of Mathematical and Physical Sciences, Faculty of Science, University of Technology Sydney, Sydney, NSW, 2007, Australia

^c Australian Institute of Innovative Materials, Innovation Campus, Squires Way, University of Wollongong, North Wollongong, NSW, 2500, Australia

Email: shenglizhai@jiangnan.edu.cn

E-mail: guoxiu.wang@uts.edu.au

1. Experimental Procedures

1.1 Preparation of GF@APTS

For the condensation of APTS on GF, commercial GF roll was immersed in an aqueous solution containing 2.5 wt% anhydrous ethanol and 3 wt% 3-Aminopropyltriethoxysilane (APTS)^[1], and continuously, slowly drawn out by a rotating collector. The silanol groups from hydrolyzed APTS undergo condensation reactions either with each other or with hydroxyl groups on the glass surface, resulting in the formation of Si-O-Si bonds. This process allows APTS to anchor onto the GF surface while simultaneously creating a siloxane network between individual glass fibers. The condensation layer was dried after passing a heating fan. The resulting GF@APTS was further dried in air for 12h.

1.2 Synthesis of NVO cathode

All raw materials used in this experiment are analytically pure. In a typical synthesis operation, 0.4547 g vanadium pentoxide was added into 50 ml DI water and stirred for 1 hour at room temperature. Subsequently, 4 ml diluted hydrogen peroxide was poured into the vanadium-containing solutions. After stirring for 5 h to form an orange solution, 0.12 g of sodium hydroxide was added, and the mixture was stirred for an additional 2 h. Finally, the solutions were transferred to a 50 mL autoclave with a Teflon liner and maintained at 180 °C for 12 h. After cooling down to room temperature, the samples were washed several times with DI water and ethanol and dried at 60 °C to obtain NVO cathode.^[2]

1.3 Electrochemical Measurements

Zn, Cu foils, as well as NVO-coated stainless steel mesh (SS@NVO), were punched into circular disks with a diameter of approximately 1.4 cm. The Zn disks were then polished with sandpaper and rinsed with water to remove passivation layers and simultaneously smooth the surface. The polished Zn and Cu disks were referred to as bare Zn and Cu electrodes, respectively. The NVO slurry was prepared by mixing 70% NVO, 20% Ketjen Black, and 10% PVDF, using N-methyl-2-pyrrolidone (NMP) as the solvent. This mixture was uniformly coated onto a stainless-steel mesh and vacuum-dried at 60 °C for 12 h to obtain SS@NVO cathode. 2M ZnSO₄ was used as the electrolyte with a pH value of ~4.3. Electrochemical performance for all samples was assessed by assembling CR2032-type coin cells. The batteries were assembled at room temperature and allowed to rest for 6 h prior to

electrochemical measurements. For the pouch cells, the positive and negative electrode materials were symmetrically positioned on either side of the separator, followed by the introduction of a sufficient volume of electrolyte. The cells were then heat-sealed within a pouch. Electrochemical impedance spectroscopy (EIS), cyclic voltammetry (CV), and chronoamperometry (CA) measurements were conducted using a VersaSTAT 3F electrochemical workstation. Additionally, linear sweep voltammetry (LSV) and Tafel plots were measured using a CHI660E electrochemical workstation (Shanghai, CH Instruments). Rate capability, cycle performance, and galvanostatic charge/discharge (GCD) measurements were performed using a CT3002A Land Battery system (Wuhan, China).

1.4 Material Characterization

The microstructure and elemental mapping of the samples were analyzed with a Cold Field Emission Scanning Electron Microscope (FESEM, Regulus 8100). Chemical compositions were characterized using FESEM coupled with energy-dispersive X-ray spectroscopy (EDS) and a Kratos Axis UltraDLD X-ray photoelectron spectrometer (XPS). All XPS spectra were calibrated to the adventitious hydrocarbon (AdvHC) carbon peak at 284.8 eV. Fourier-transform infrared (FTIR) spectra were obtained using a Nicolet 6700 spectrometer in attenuated total reflectance (ATR) mode. The pore sizes of the various separators were calculated using a Capillary Flow Porometer (CFP-1100A, Stowell Inc., USA). Tensile stress and strain curves were assessed using Models ESM303 and ESM303H Test Stands (Mark-10, USA). The puncture resistance was measured using a Lloyd Instruments testing system (AMETEK, USA). The zeta potential values were measured with a Nano-ZS90 zeta potential analyzer (Malvern, UK). X-ray diffraction (XRD) patterns were recorded using a D2 PHASER X-ray diffractometer (Bruker, Germany). Raman spectra were obtained using a microscopic confocal laser Raman spectrometer (Renishaw, UK). Solid-state ^{29}Si Nuclear magnetic resonance (NMR) spectra were recorded on Bruker NMR Spectrometer (AVANCEIII/WB-400).

1.5 XAFS measurement and analysis

Zn K-edge XAFS spectra were collected on the BL13SSW beamline at Shanghai Synchrotron Radiation Facility (SSRF). The data about the Zn K-edge ($E = 9659$ eV) were collected at room temperature in transmission mode. The Athena software package was used to process the raw data.

1.6 Computational modeling

Heat transfer simulation: In this study, thermal conduction through separators at a high temperature of 1298.15 K (1025 °C) was simulated using COMSOL Multiphysics. A three-dimensional model was constructed for different separator materials. The dimension of the model was 5 cm × 2 cm × 1 cm based on the size of the real separators undergoing burning test. The simulation applied a constant temperature boundary condition of 1298.15 K to the lower side of the model, while the opposite side was exposed to ambient air at 298.15 K (25 °C), with a convective heat transfer coefficient of 15 W/(m²·K). The initial temperature across the separator was set to 298.15 K. The "Heat Transfer in Solids" physics module was used to model the conduction process, employing a time-dependent solver with a time step of 1 second to simulate heat conduction over a 30 seconds duration.

Density functional theory (DFT) calculation and molecular dynamics (MD) simulation: All the DFT calculations were performed using the Materials Studio. The structural optimization was performed through the open-source CASTEP module. All calculations employed the GGA-PBE functional. The system's charge was set to reflect actual conditions, ensuring non-polarized spin polarization. An electronic energy cutoff of 320 eV was applied, along with a k-point grid of 2 × 2 × 1. Ultra-soft pseudopotentials were utilized, and the relativistic treatment followed the Koelling-Harmon method, with a self-consistent field (SCF) tolerance of 2×10⁻⁶ eV/atom. The pseudopotentials employed are ultra-soft, with relativistic treatment based on the Koelling-Harmon method. The self-consistent field (SCF) tolerance is set to 2×10⁻⁶ eV/atom. The adsorption energy (E) between two species is calculated as follows: $E = E_{ab} - E_a - E_b$ where E_{ab} is the total energy of the combined system, and E_a and E_b are the energies of the two species. Classical MD simulations were performed in Materials Studio 2020 using COMPASS force-field parameters. To replicate the realistic electrolyte GF@APTS interface, we built a three-layer model in which the bottom layer is the GF, the middle layer consists of APTS molecules grafted onto the GF surface, and the top layer contains the ZnSO₄ aqueous electrolyte.

2. Supplementary Figures and Tables

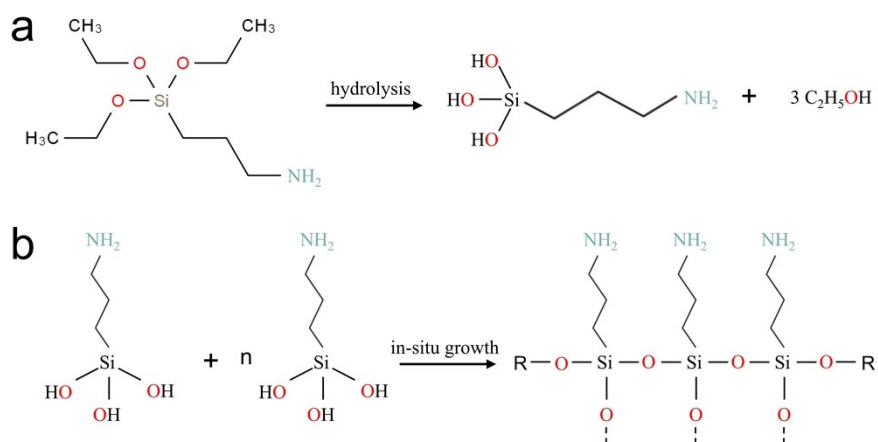


Figure S1. (a) Schematical outline of the hydrolysis process of the 3-Aminopropyltriethoxysilane, producing silanol groups (Si-OH). (b) The condensation between silanol groups and glass fiber (GF). The newly formed silanol groups condense with the hydroxyl groups on the GF surface (Si-OH from the glass fiber), forming strong covalent Si-O-Si bonds. This results in the coupling agent being chemically bonded to the GF surface, the obtained separators were denoted as GF@APTS.

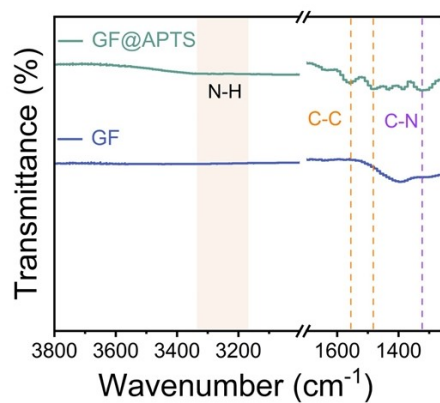


Figure S2. FTIR spectra of GF and GF@APTS separators.

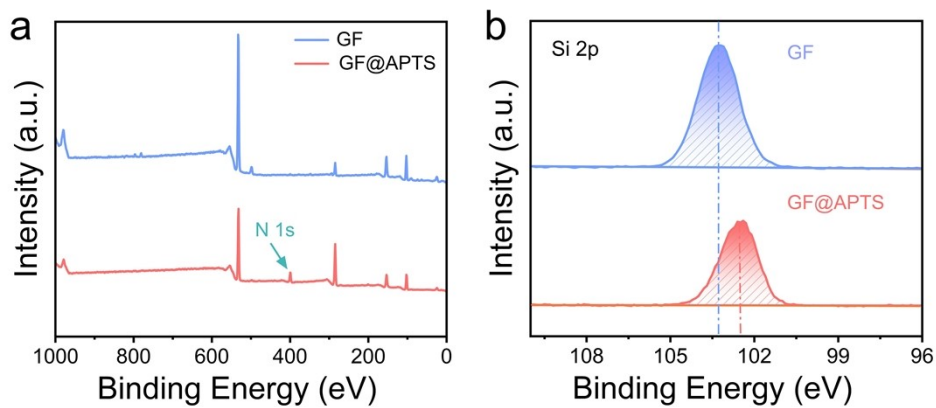


Figure S3. (a) XPS survey scan and (b) high-resolution Si 2p spectra of GF and GF@APTS separators.

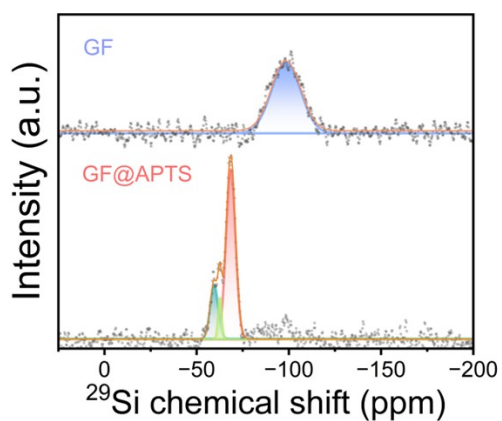


Figure S4. Solid-state ^{29}Si NMR spectra of GF and GF@APTS separators.

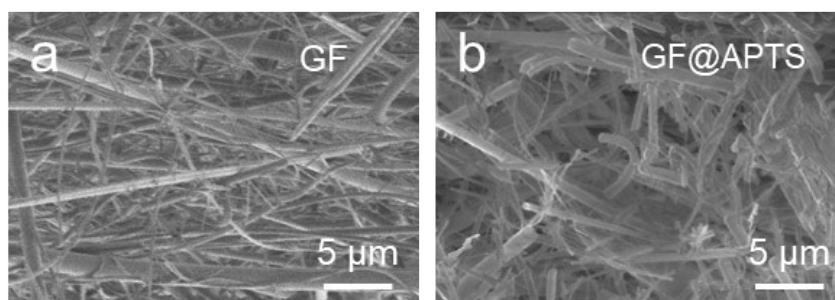


Figure S5. Cross-sectional SEM images of (a) GF and (b) GF@APTS separators.

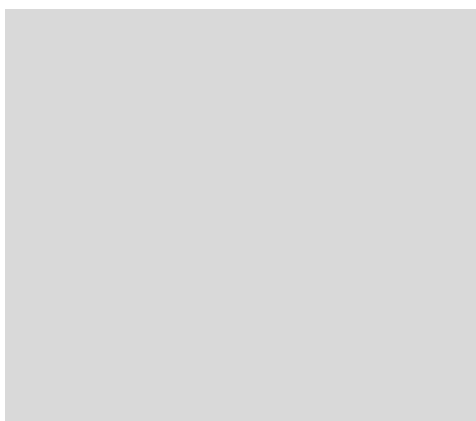


Figure S6. Pore size distribution of GF and GF@APTS separators.

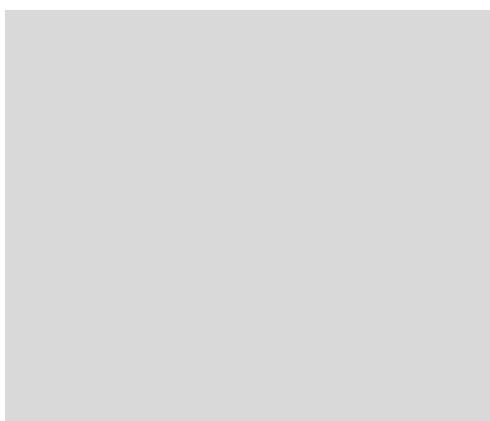


Figure S7. Tensile strength of GF and GF@APTS separators.



Figure S8. Puncture test of GF and GF@APTS separators.

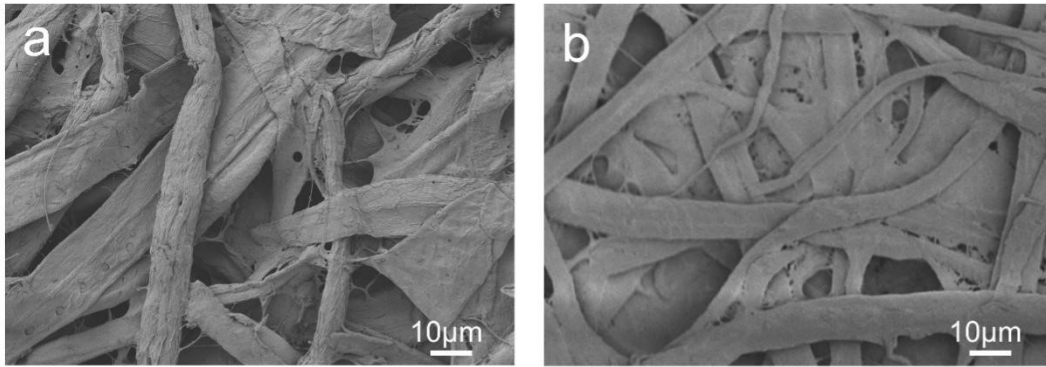


Figure S9. SEM images of a piece of (a) cellulose nanofiber separator (CF) and (b) CF@APTS separator.

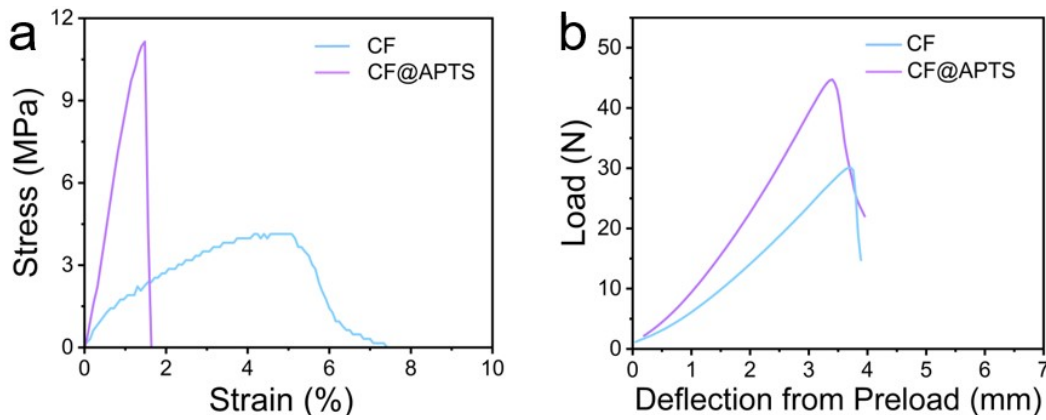


Figure S10. (a) Tensile strength and (b) puncture test of cellulose nanofiber separators (CF) and CF@APTS separators.

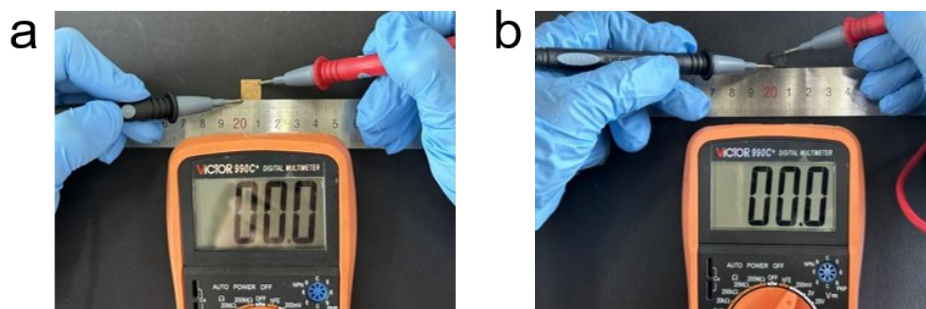


Figure S11. Electrical conductivity measurement of (a) GF@APTS after burning test and (b) thermal stability test.

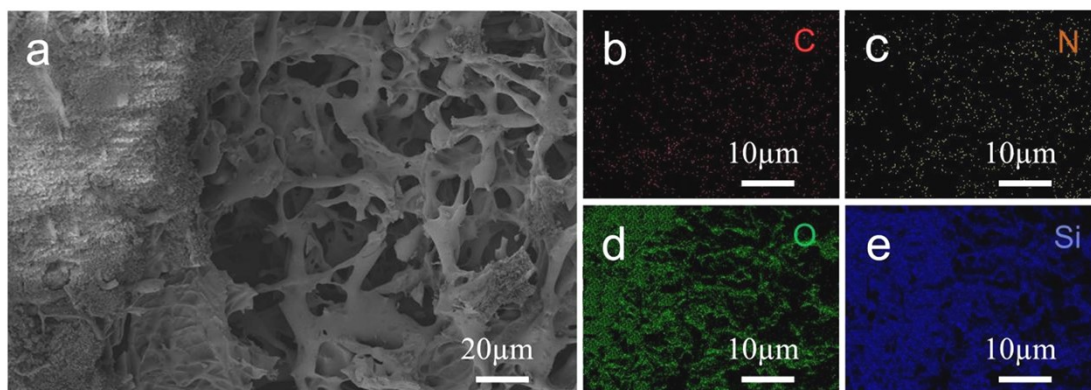


Figure S12. (a) SEM images and (b) EDS mapping of burned GF@APTS.

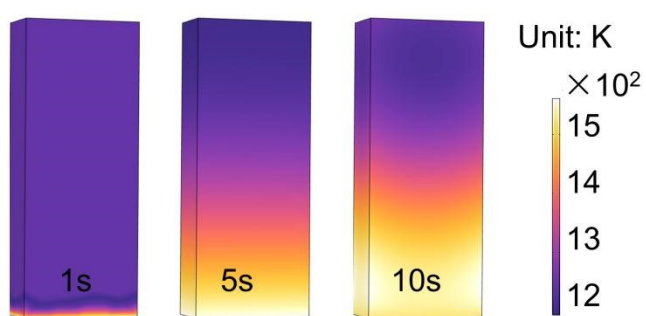


Figure S13. Heat transfer simulation in carbon-based materials.

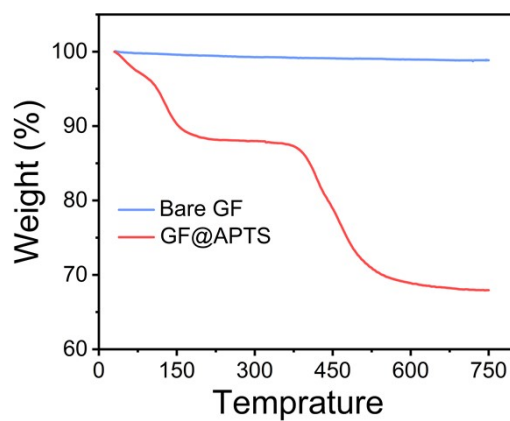


Figure S14. TGA curves of separators.

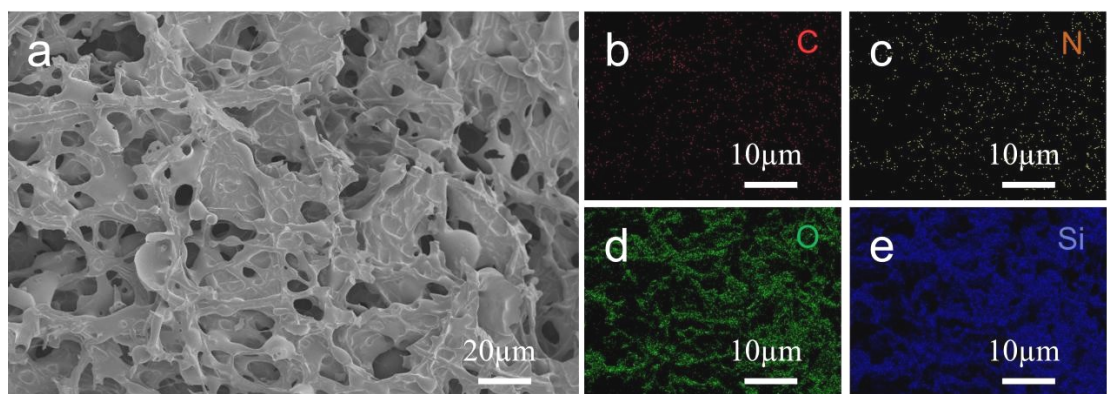


Figure S15. SEM and EDS elemental mapping of GF@APTS after thermal stability test.

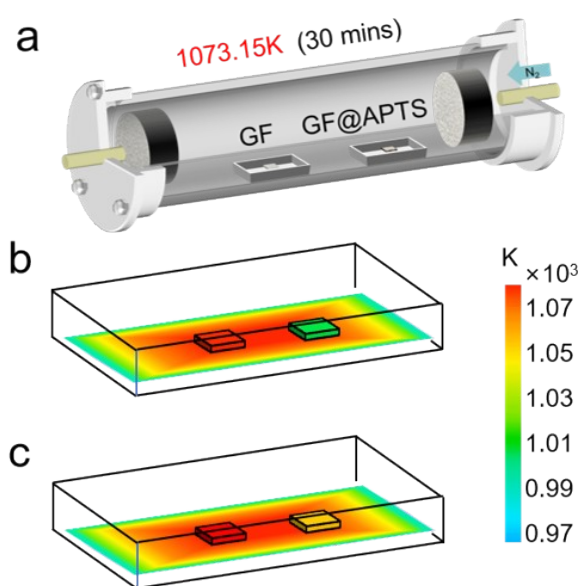


Figure S16. Simulating the heat transfer within a tube furnace for 30 mins (a). Heat transfer simulation with GF (left) and GF@APTS (right) separators at 800 °C (1073.15 K) for 1 min (b) and 30 mins (c).

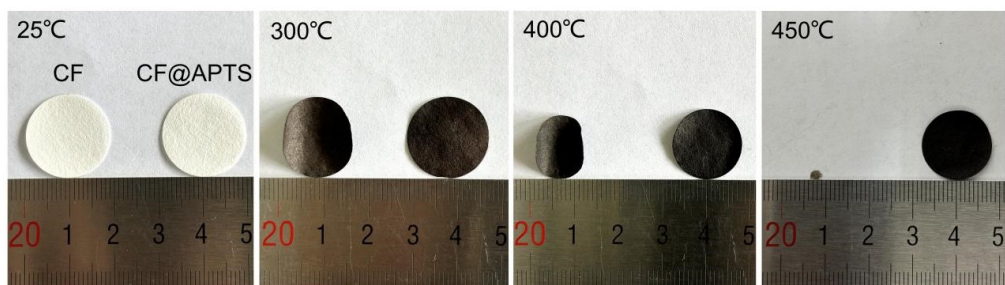


Figure S17. The thermal stability test of CF and CF@APTS separators at various temperatures.

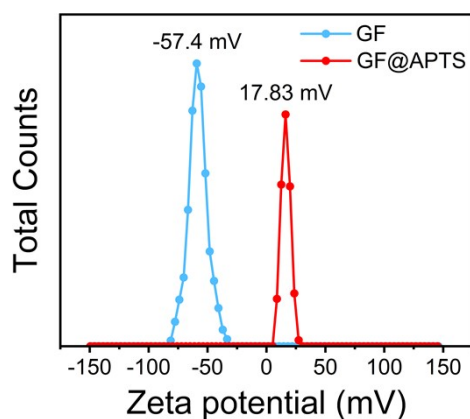


Figure S18. The zeta potential of separators.

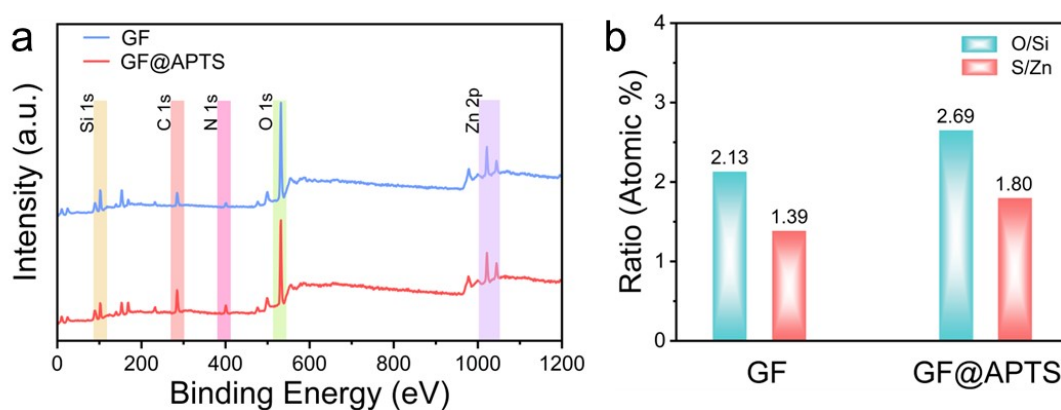


Figure S19. (a) XPS spectra of ion-adsorbed separators and (b) corresponding atomic ratio between various elements. GF and GF@APTS separators were soaked in 2M ZnSO₄ solution for 3 hours to fully absorb ions. Subsequently, they were rinsed with DI water and dried in the room temperature before characterization.

Overall, according to XPS spectra, the O/Si ratio increases by 26.3% upon APTS grafting (from 2.13 for pristine GF to 2.69 for GF@APTS), confirming conversion of the SiO₂-dominated surface to a silanol-rich polysiloxane network. In addition, APTS modified separators can adsorb over twice as many Zn²⁺ and SO₄²⁻ compared to the bare GF separators when presenting in 2M ZnSO₄ electrolyte (see Figure 3d). The S/Zn ratio rises by 29.5% (from 1.39 to 1.80), indicating enhanced SO₄²⁻ adsorption on the amine-functionalized surface.

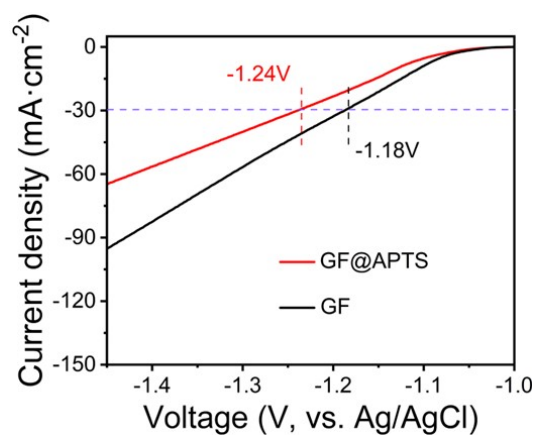


Figure S20. Linear sweep voltammetry curves in 2M ZnSO₄ as electrolyte. The HER onset potential when using different separators are -1.24 and -1.18 V, respectively.

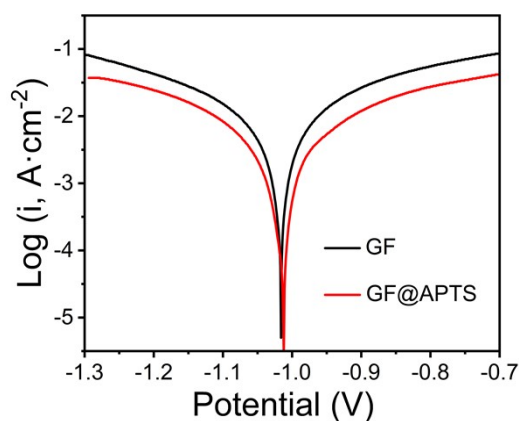


Figure S21. Tafel curves showing the corrosion behaviors in the 2M ZnSO₄ electrolytes when using two types of separators.

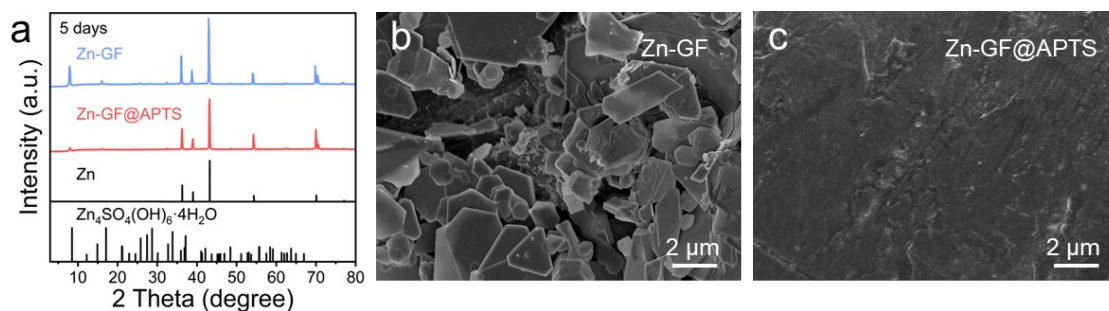


Figure S22. (a) XRD patterns and (b, c) SEM images of the Zn electrodes disassembled from Zn//Zn symmetric cells under 5-days shelf time.

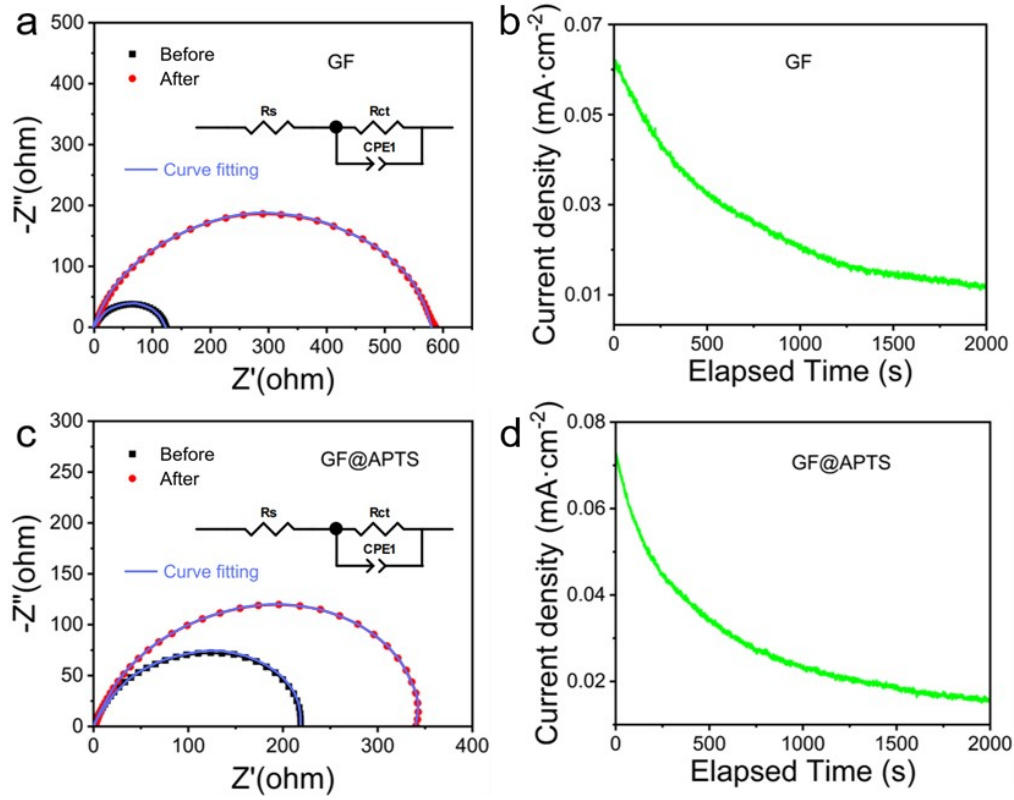


Figure S23. (a, c) Nyquist plots at the initial and steady states and (b, d) CA curves of the Zn//Zn cells.

Determination of the Zn^{2+} transference number within separators.

The symmetric Zn//Zn cells with two types of separators were assembled to measure the Zn^{2+}

transference number ($t_{Zn^{2+}}$) based on the following equation:

$$t_{Zn^{2+}} = \frac{I_s(\Delta V - I_o R_o)}{I_o(\Delta V - I_s R_s)}$$

where the I_o and I_s are the initial and steady-state current, respectively, obtained from CA test, and ΔV is the constant potential (25 mV). R_o and R_s are the interface impedances before and after the CA test, respectively. The transference number of GF and GF@APTS separators were calculated to be 0.26 and 0.667, respectively.

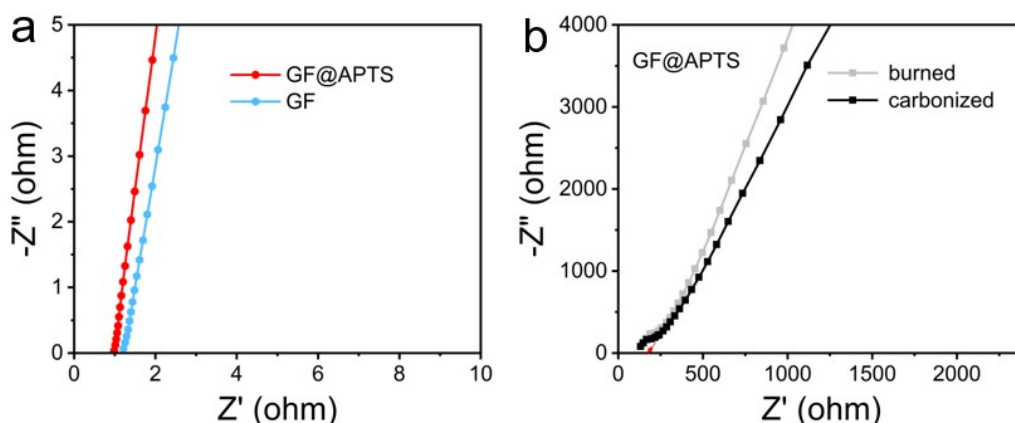


Figure S24. (a) Nyquist plots of the symmetric stainless-steel (SS) cells with GF and GF@APTS separators, (b) GF@APTS after burning and thermal stability test.

Determination of ionic conductivity (σ):

The ionic conductivity of separators were determined by electrochemical impedance spectroscopy (EIS) using AMETEK VERSA STAT 3F electrochemical workstation. The EIS was performed on a SS/separator/SS symmetric cells with 2M ZnSO₄ electrolyte. The EIS frequency range was from 0.1 Hz to 10⁶ Hz and the amplitude was 10 mV. The real impedance at the highest frequency was taken as the bulk resistance. The ionic conductivity (σ) of the separator was calculated according to the following equation:

$$\sigma = \frac{d}{R_b S}$$

Where d represent the thickness of the separator, R_b represent bulky resistance, and S represent effective area of the separator. The ionic conductivity of the GF, GF@APTS, and burned GF@APTS separators is 8.660, 12.700, and 0.054 mS·cm⁻¹, respectively.

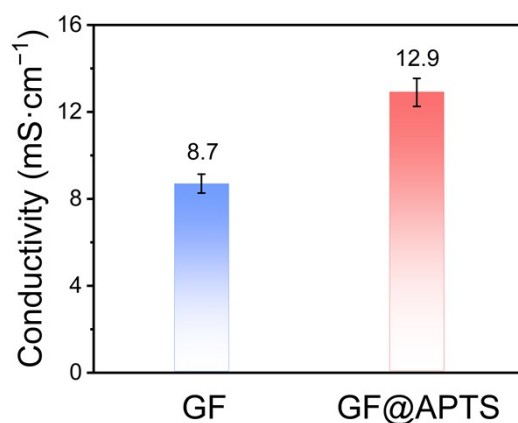


Figure S25. The ionic conductivity of two different separators.

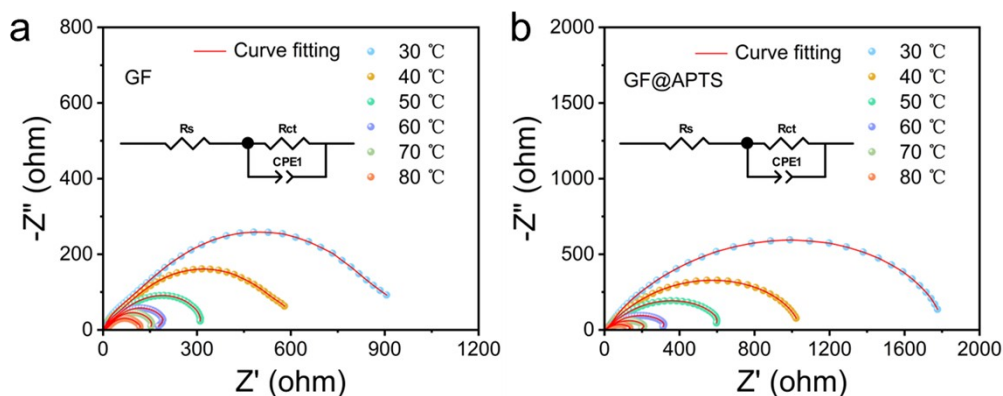


Figure S26. Nyquist plots of the Zn//Zn cell with (a) GF and (b) GF@APTS separators at different temperatures.

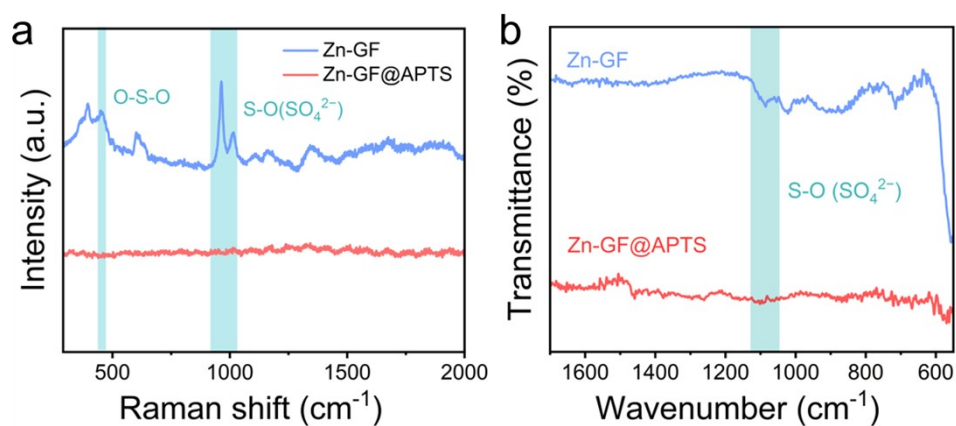


Figure S27. (a) Raman and (b) FTIR spectra of Zn electrodes with different separators in Zn//Zn symmetric cells after cycling.

Both Raman and FTIR analyses reveal the characteristic vibrational modes of $\text{Zn}_4\text{SO}_4(\text{OH})_6 \cdot 4\text{H}_2\text{O}$. In the Raman spectra, the intense band centered at 1002 cm^{-1} is assigned as the symmetric S-O stretching vibration of SO_4^{2-} tetrahedra. The frequencies at 452 and 474 cm^{-1} belong to the symmetric bending (O-S-O) vibrations. In the FTIR spectra, S-O stretching vibrations are observed at $1050\text{-}1200 \text{ cm}^{-1}$ bending modes. Raman, FTIR together with XRD results confirms the presence of $\text{Zn}_4\text{SO}_4(\text{OH})_6 \cdot 4\text{H}_2\text{O}$ by-product.

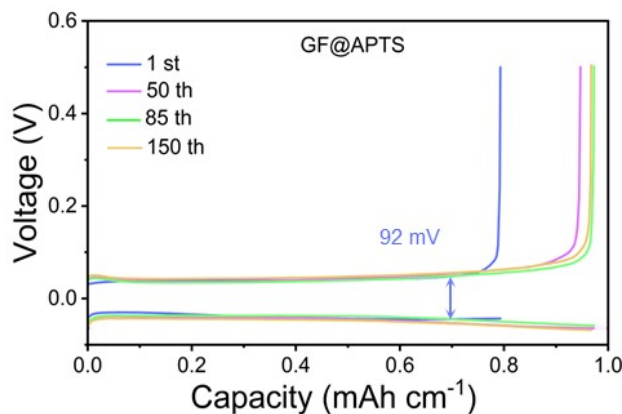


Figure S28. Voltage profiles of the Zn//Cu cell with GF@APTS separator at various cycles.

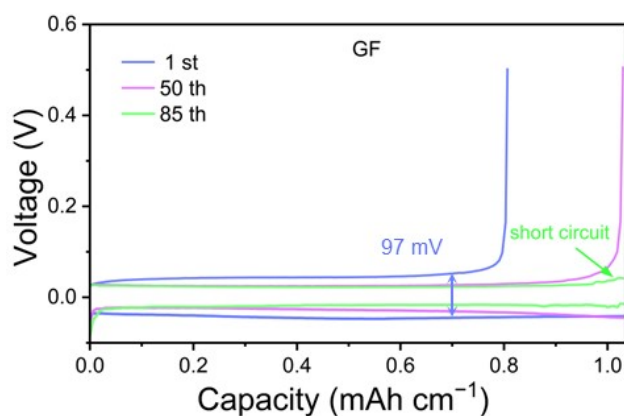


Figure S29. Voltage profiles of the Zn//Cu cell with GF separator at various cycles.

In the first cycle, the nucleation overpotential of the cell with the GF separator was slightly higher (~97 mV) compared to that of the cell with the GF@APTS separator (~92 mV), suggesting a marginally lower initial nucleation and deposition barrier for Zn on the APTS-modified surface. However, in subsequent cycles, the cell utilizing the bare GF separator exhibited a progressive decline in the voltage gap between Zn plating and stripping, eventually leading to an abrupt voltage drop which is indicative of cell failure. This behavior resembles the “soft short circuit” phenomenon frequently reported in metal-ion batteries.^[3] As suggested in recent literature, such soft shorts can originate from localized zinc dendrites or porous “dead Zn” structures that momentarily bridge the separator, particularly under high-rate cycling conditions. As cycling continues, zinc dendrites progressively grow and can eventually pierce the separator, leading to internal short circuits and cell failure. In contrast, the GF@APTS-based cell maintained stable voltage profiles over extended cycling, likely due to more uniform Zn²⁺ deposition and a reduced nucleation barrier imparted by the amine-functionalized surface.

This surface modification helps to minimize localized deposition hot spots and suppress the formation of transient conductive pathways, thereby mitigating soft short circuits and contributing to lower long-term overpotential in Zn symmetric cells.

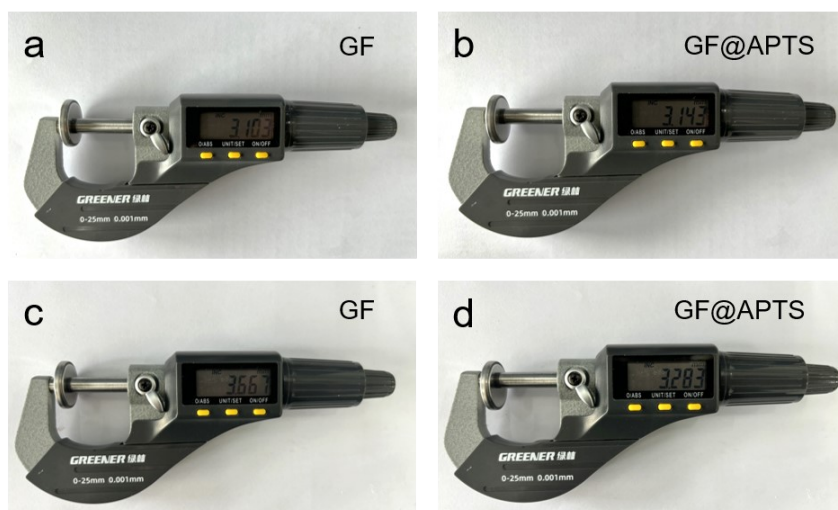


Figure S30. The thickness variation of symmetric Zn cells with different separators before (a, b) and after (c, d) long-term cycling.

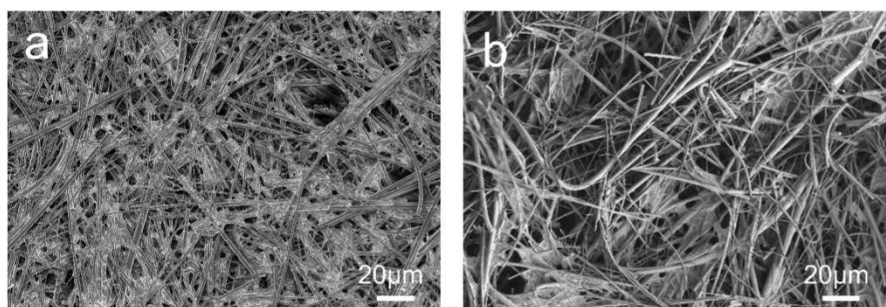


Figure S31. SEM images of (a) GF and (b) GF@APTS separators in Zn//Zn symmetric cells after long-term cycling. Many dead Zn appeared in the bare GF separators, while the GF@APTS remains clean.

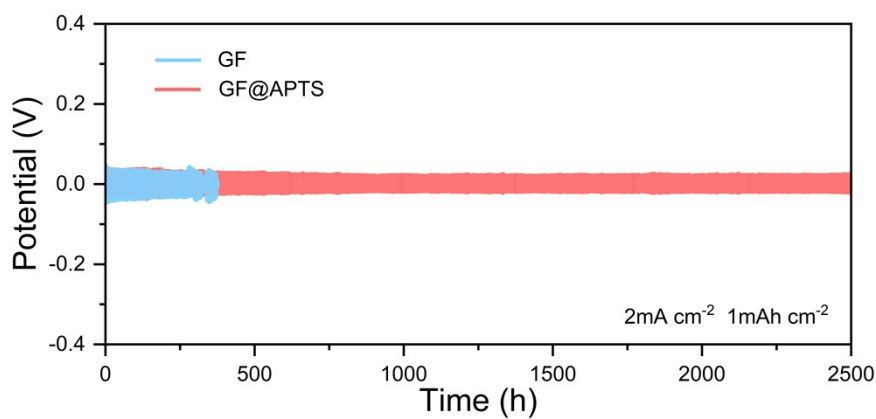


Figure S32. Long-term galvanostatic Zn plating/stripping curves at 2 mA cm^{-2} with a limited capacity of 1 mAh cm^{-2} .

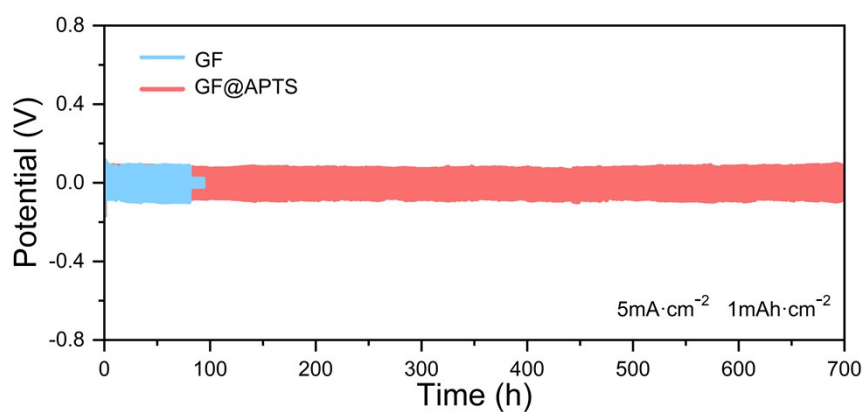


Figure S33. Long-term galvanostatic Zn plating/stripping curves at 5 mA cm^{-2} with a limited capacity of 1 mAh cm^{-2} .

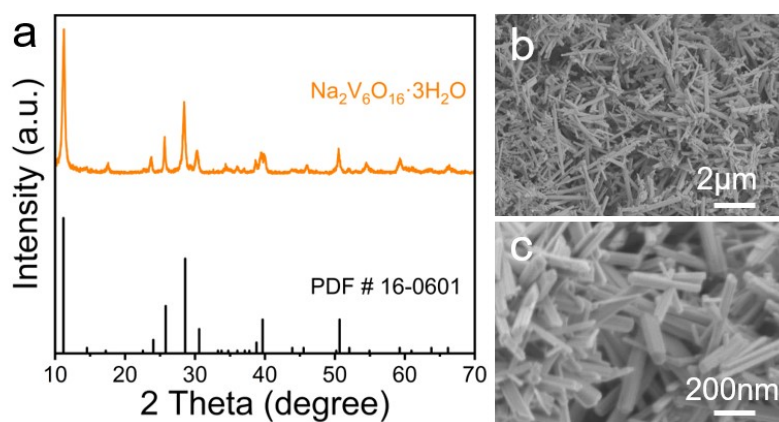


Figure S34. (a) XRD pattern and (b, c) SEM images of the $\text{Na}_2\text{V}_6\text{O}_{16} \cdot 3\text{H}_2\text{O}$ cathode material.

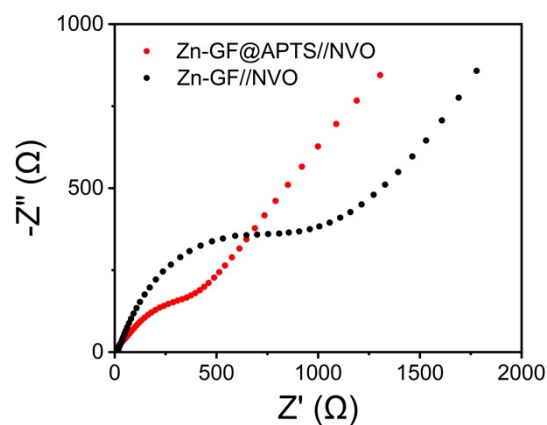


Figure S35. The Nyquist plots of the full cell after long-term cycling.

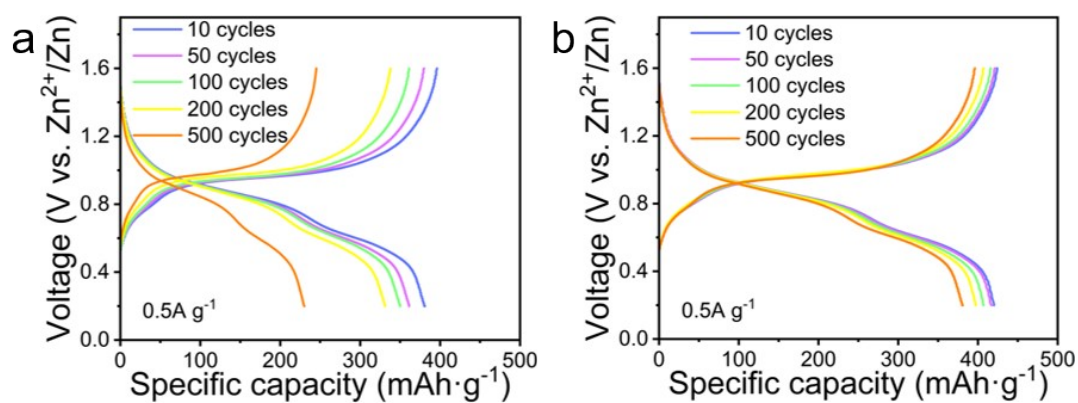


Figure S36. Voltage profiles of Zn//NVO full cells when using (a) bare GF separators and (b) GF@APTS separators during long-term cycling.

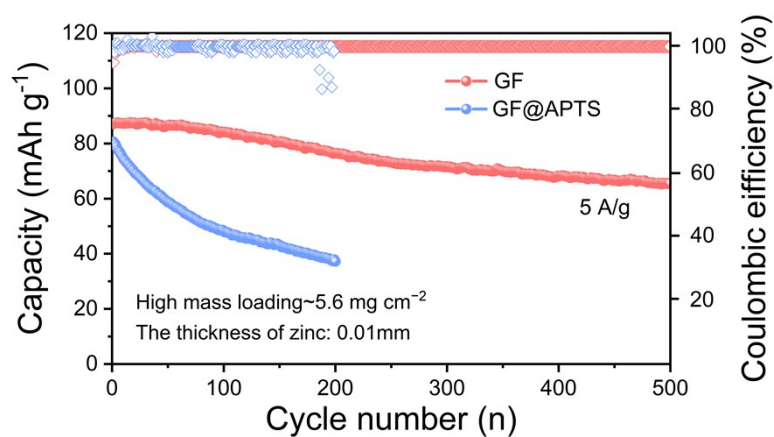


Figure S37. Capacities of Zn//NVO full cells with high mass loading cathode and thin Zn sheet anode.

Employing high mass-loading cathodes and low negative-to-positive (N/P) capacity ratios is essential for assessing real-world applicability. Full-cell tests using cathodes with a significantly increased mass loading of 5.6 mg cm^{-2} (compared to the previous 1.1 mg cm^{-2}), paired with ultra-thin Zn anodes of 0.01 mm thickness (previously 0.11 mm), effectively achieving lower N/P ratios. The cells were cycled at a current density of 5 A g^{-1} . As shown in the Figure S37, full cells assembled with the GF@APTS separator exhibit excellent cycling stability, retaining high capacity over 500 cycles. In contrast, cells with unmodified GF separators exhibited pronounced capacity loss from the initial cycles and a sharp decline in coulombic efficiency after 200 cycles. These results strongly demonstrate the superior electrochemical performance and robustness of the GF@APTS separator under low N/P-ratio conditions, showing great practical application potential.

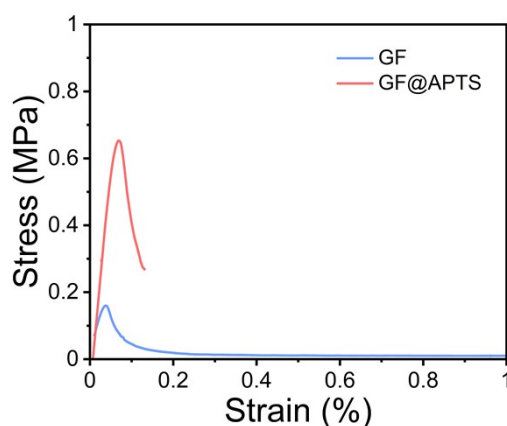


Figure S38. Tensile strength of GF and GF@APTS separators disassembled from pouch cells after cycling.

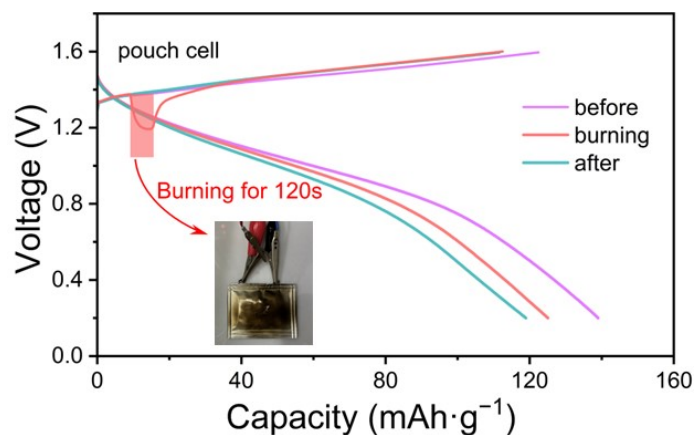


Figure S39. GCD profiles of Zn//NVO pouch cells when exposed to flame.

When the cells were cycled at 5 A g^{-1} and subjected to a 120 s flame during the charging step, a transient voltage drop was observed. However, the voltage was fully recovered once the flame was removed. In the subsequent cycle, the cells retained 85.6% of their original capacitance prior to the flame test, demonstrating excellent flame-resistance.

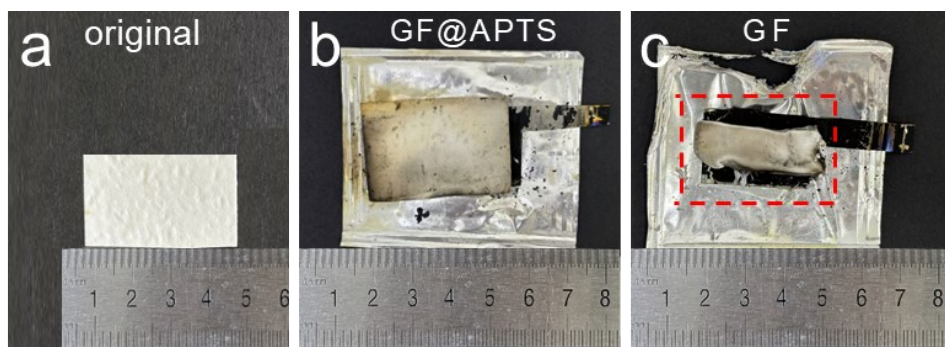


Figure S40. Optical images of (a) original separators, burned pouch cells with (b) GF and (c) GF@APTS separators. The temperature beneath the aluminum-plastic film was measured to be approximately 700-780 °C.

Table S1. Comparison of various separator design strategies for stabilizing Zn anodes in ZIBs.

Separator	Current density / areal capacity	Lifespan	Ref.
GF@APTS	0.2 mA cm ⁻² /0.2 mAh cm ⁻²	7000 h	This work
	2 mA cm ⁻² /1 mAh cm ⁻²	2500 h	
	5 mA cm ⁻² /1 mAh cm ⁻²	700 h	
Cellulose film	2 mA cm ⁻² /4 mAh cm ⁻²	850 h	[4]
ZrO ₂ @cellulose film	0.5mA cm ⁻² /0.25 mAh cm ⁻²	2000 h	[5]
N-graphdiyne@	3 mA cm ⁻² /1 mAh cm ⁻²	600 h	[6]
cellulose film	5 mA cm ⁻² /1 mAh cm ⁻²	500 h	
CF-SO3	2 mA cm ⁻² /4 mAh cm ⁻²	1200 h	[7]
PNGF	3 mA cm ⁻² /1.2 mAh cm ⁻²	1250h	[8]
TS-GF	5mA cm ⁻² /2 mAh cm ⁻²	860 h	[9]
LC@UiO-66	2 mA cm ⁻² /2 mAh cm ⁻²	700 h	[10]
Bamboo cellulose	1 mA cm ⁻² /1 mAh cm ⁻²	1600 h	[11]
	2 mA cm ⁻² /1 mAh cm ⁻²	600 h	
Filter paper	1 mA cm ⁻² /1 mAh cm ⁻²	400 h	[12]
PANI-GF	2 mA cm ⁻² /1 mAh cm ⁻²	560 h	[13]
CT (cotton towel)	1 mA cm ⁻² /0.5 mAh cm ⁻²	1200 h	[14]

Table S2. Comparison of the cycling performance of ZIBs.

Separator	Cathode material	Cycle number	Capacity retention	Ref.
GF@APTS	$\text{Na}_2\text{V}_6\text{O}_{16}\cdot 3\text{H}_2\text{O}$	10000	84.8%	This work
ZrO ₂ @cellulose film	MnO ₂	3000	87.2%	[5]
N-graphdiyne@ cellulose film	V ₆ O ₁₃	2000	75%	[6]
CF-SO ₃	MnO ₂	1500	85.1%	[7]
PNGF	LMO	400	65%	[8]
TS-GF	LiMn ₂ O ₄	300	71.3%	[9]
LC@UiO-66	MnO ₂	1000	70.3%	[10]
Bamboo cellulose	MnO ₂	1000	31%	[11]
Filter membrane	$\text{Na}_2\text{V}_6\text{O}_{16}\cdot 3\text{H}_2\text{O}$	5000	83.8%	[12]
PANI-GF	MnO ₂	1000	62.6%	[13]
CT (cotton towel)	MnO ₂	2400	~33%	[14]

References

- 1 A. Zheng, H. Wang, X. Zhu, S. Masuda, *Compos. Interfaces*, 2002, **9**, 319-333.
- 2 S. Li, X. Xu, K. Wang, W. Chen, X. Lu, Z. Song, J.-Y. Hwang, J. Kim, Y. Bai, Y. Liu, *ACS Energy Lett.*, 2022, **7**, 3770-3779.
- 3 Q. Li, A. Chen, D. Wang, Z. Pei, C. Zhi, *Joule*, 2022, **6**, 273-279.
- 4 W. Zhou, M. Chen, Q. Tian, J. Chen, X. Xu, C.-P. Wong, *Energy Storage Mater.*, 2022, **44**, 57-65.
- 5 J. Cao, D. Zhang, C. Gu, X. Zhang, M. Okhawilai, S. Wang, J. Han, J. Qin, Y. Huang, *Nano Energy*, 2021, **89**, 106322.
- 6 Q. Yang, L. Li, T. Hussain, D. Wang, L. Hui, Y. Guo, G. Liang, X. Li, Z. Chen, Z. Huang, *Angew. Chem.*, 2022, **134**, e202112304.
- 7 W. Zhou, M. Yang, M. Chen, G. Zhang, X. Han, J. Chen, D. Ma, P. Zhang, *Adv. Funct. Mater.*, 2024, **34**, 2315444.
- 8 Y. Zhang, Z. Zeng, S. Yang, Y. Zhang, Y. Ma, Z. Wang, *Energy Storage Mater.*, 2023, **57**, 557-567.
- 9 Y. Zhang, S. Yang, Y.-J. Zhu, D. Li, L. Cheng, H. Li, Z. Wang, *J. Colloid Interface Sci.*, 2024, **656**, 566-576.
- 10 H. Ma, J. Yu, M. Chen, X. Han, J. Chen, B. Liu, S. Shi, *Adv. Funct. Mater.*, 2023, **33**, 2307384.
- 11 J. Fu, H. Wang, P. Xiao, C. Zeng, Q. Sun, H. Li, *Energy Storage Mater.*, 2022, **48**, 191-191. f196.
- 12 Y. Qin, P. Liu, Q. Zhang, Q. Wang, D. Sun, Y. Tang, Y. Ren, H. Wang, *Small*, 2020, **16**, 2003106.
- 13 N. Zhao, Y. Zhang, Z. Zhang, C. Han, Y. Liang, J. Li, X. Wang, L. Dai, L. Wang, Z. He, *J. Colloid Interface Sci.*, 2023, **642**, 421-429.
- 14 P. Cao, H. Zhou, X. Zhou, Q. Du, J. Tang, J. Yang, *ACS Sustainable Chem. Eng.*, 2022, **10**, 8350-8359.